Study of femtosecond laser multi-scale textured steel surfaces on the wettability in relation to ageing

Ronny Elleb, Thierry Engel, Frédéric Antoni, Joël Fontaine, Frédéric Mermet, Fabienne Poncin-Epaillard

Study of femtosecond laser multi-scale textured steel surfaces on the wettability in relation to ageing

Ronny Elleb[1,2], Thierry Engel[2,3,4], Frédéric Antoni[4], Joël Fontaine[3,4], Frédéric Mermet[2], Fabienne Poncin-Epaillard[1,*]

[1] IMMM, Institut des Molécules et Matériaux du Mans, CNRS UMR 6283, Le Mans Université, 72085 Le Mans, France

[2] IREPA LASER, Centre de Transfert Technologique, Parc d'Innovation, 67400 Illkirch France

[3] INSA, Institut National des Sciences Appliquées, 67084 Strasbourg, France

[4] ICUBE Laboratoire des Sciences de l'Ingénieur, de l'Informatique et de l'Imagerie, UMR 7357, 67000 Strasbourg, France

*corresponding author: fabienne.poncin-epaillard@univ-lemans.fr

Abstract:

Micro and nanometric double scale structures are produced on a steel material irradiated by a femtosecond laser in order to study the alteration of the surface properties, in particular wettability. Following a texturing, the latter develops indeed from a hydrophilic to a hydrophobic state, possibly a superhydrophobic one, according to a progression which depends on multiple factors, gathered under the term ageing. Two types of grid patterns were performed on the samples to test the effect of the Gaussian laser shot overlap. In order to characterize not only the topology of the textured surfaces, but also the associated chemistry, 4 techniques were used, allowing for the analysis from the first atomic layers to those at 1 µm depth. In particular, carbon and oxygen levels were measured as a function of material, maturation time and storage conditions. We have identified two oxides, hematite and magnetite, whose presence is directly related to the energy density of the laser beam. We explain the mechanism of their formation by combining two pre-existing models: the appearance of a magnetite-active site induced by the laser and a martitization process.

Key-words: Femtosecond laser texturation, Steel, Multi-scale structure, Wettability, Ageing, Surface chemistry

1. Introduction

In the past decades, most of the published studies were focused on comprehensive studies of interfacial behavior between solids and liquids [1]. Specifically, the superhydrophobicity of material surfaces based on a multi-scale bio-inspired morphology is of high interest for both fundamental and applied research. Such a surface behavior can be achieved by chemical etching [2], nanoparticle dispersion [3], plasma deposition or etching [4-5], electroless plating [6] and photolithography [7]. Dealing with metallic substrates, the superhydrophobic property is obtained owing to material processes using both nanosecond or femtosecond laser patterning and (electro)chemical coating [8-12]. More precisely, in order to reach the superhydrophobic state on metallic surfaces, which corresponds to values of WCA (water contact angle) above 150° with the lowest contact angle hysteresis, double scale hierarchical structures are to be built. The latter can

be obtained through laser texturing leading to a composite solid-air-liquid interface. Hence, the contact area between droplets and surface decreases, and so do the surface adhesive properties [13].

One may also achieve a non-wetting effect with water by texturing a metal surface with a nanosecond laser [14-15] or with a femtosecond laser [16-21]. In both cases, the very first effect of laser texturing is to drastically reduce the surface WCA down to the hydrophilic state. After irradiation, the WCA evolves over time to reach hydrophobicity or even superhydrophobicity in several cases [19-21]. This phenomenon is commonly known as ageing. Investigations on wettability evolution are mainly carried out in the literature from the chemical perspective [15-22] as the fresh surface goes through chemical reactions with the environment [23].

After laser interaction, the carbon and oxygen concentrations change without the possibility to precisely determine the element or the reliable mechanism of the wettability alteration. Several authors, including Bizi-Bandoki *et al*. [17], mentioned an increase of oxide concentration as well as a decrease of the carbon amount, in order to explain the transition from hydrophilic to hydrophobic state, while other authors such as Kietzig *et al.* [18], put forward the hypothesis that the chemical maturation is bound to the carbon proportion increase on surface by CO_2 adsorption correlatively with the decrease of oxygen amount.

Several ageing studies were run under controlled, reactive or neutral environments, or even under vacuum [23], [24]. Annealing is a further technique described in [22], [24]. These various types of storage conditions are useful to evaluate the impact of air, pollutants and humidity on WCA separately. Most of the publications are in concern with the ambient air moisture, as in our case.

In this study, several analyses were used to monitor the wettability, and also to determine the proportions of chemical elements present on the surface (EDX) as well as on the extreme surface (XPS). Last, the type of oxidation generated after femtosecond laser irradiation is analyzed by Raman spectroscopy. In this paper, special attention is focused on the evolution of surface wettability, correlating WCA measurements with chemical maturation with respect to the laser-generated method of ablation. Knowledge of the chemical nature of formed oxides and their

appearance mechanisms is an important step in order to understand the non-quite clear role of carbon and oxygen.

2. Experimental part

2.1. Material

In this work, the sample is made of a 40CMD8+S steel, commonly used in mold industry. According to the manufacturer's datasheet (Table 1), in addition to its 95.95% iron content, the bulk consists of several other elements such as 1.90% chromium, 1.50% magnesium, 0.4% carbon, 0.20% molybdenum and 0.05% sulphur.

Table 1: composition of 40CMD8+S Steel.

Element	Fe	Cr	Mg	C	Mo	S
Proportion (%)	95.95	1.9	1.5	0.4	0.2	0.05

Samples with a thickness of 5 mm are treated without prior polishing. Their initial roughness Ra is around 0.3 µm.

All the samples are ultrasonically cleaned for 5 min in a solution composed of 50% acetone (CAS No. 0067-64-1) and 50% ethanol (CAS No. 0064-17-5). Then they are rapidly dried under a hot air flux to avoid any trace of pollution or organic contamination. Considering the frequent presence of non-adherent oxides on top of laser textured surfaces, the ultrasonic post-treatment allows for an increase the repeatability of the measurements.

The removal of protective layer from the steel surface (e.g. machining oil from manufacturing) will lightly and locally induce oxidation after a few months of storage in the humid ambient air, which may affect the ageing study. In order to estimate the impact of this slow natural oxidation, an analysis of the evolution of WCA was carried out for 5 months. According to Table 2, we did not notice a significant evolution. The discrepancies in the values are mainly related to

the inhomogeneity of the surface. Indeed, the deposition of a water drop on a steel irreversibly alters the contact area. Each value of WCA is an average of 3 separate measurements.

Table 2: Evolution of the contact angle of a drop of water on a 40CMD8+S steel surface stored in ambient air under 40% humidity over 5 months.

Time (month)	1	2	3	4	5
WCA (°)	77.8 ± 0.8	88.0 ± 1.7	88.5 ± 0.4	96.2 ± 0.9	91.6 ± 1.7

2.2. Laser texturing and maturation methods

Laser surface texturing was performed with an ultrafast pulsed fiber laser process (Tangerine, from Amplitude Systèmes). It delivers pulses around 300 fs duration at 1030 nm with a 250 kHz repetition rate. The mean laser power was reduced to 1 W which corresponds to a fluence of 0.56 J.cm^{-2} for a Gaussian beam profile and a spot size of 30 µm. The texturing of samples was ensured with a galvo head XY scanner and the prepared patterns are close to the lotus leaves morphology [1]. The grid consists of ablated lines called “trenches”, spaced 25 µm or 40 µm apart along both X and Y axes. The aim was to generate a multi-scale array of protrusions in two distinct ways, in order to compare the effect of a complete irradiated samples with samples presenting un-textured zones with low or zero energy densities due to the Gaussian profile of the laser beam (Fig. 1). Consequently, a first grid (G40) was prepared without trench overlap (40µm pitch grid), and a second one (G25) was made with a 20% trench overlap (25µm pitch grid).

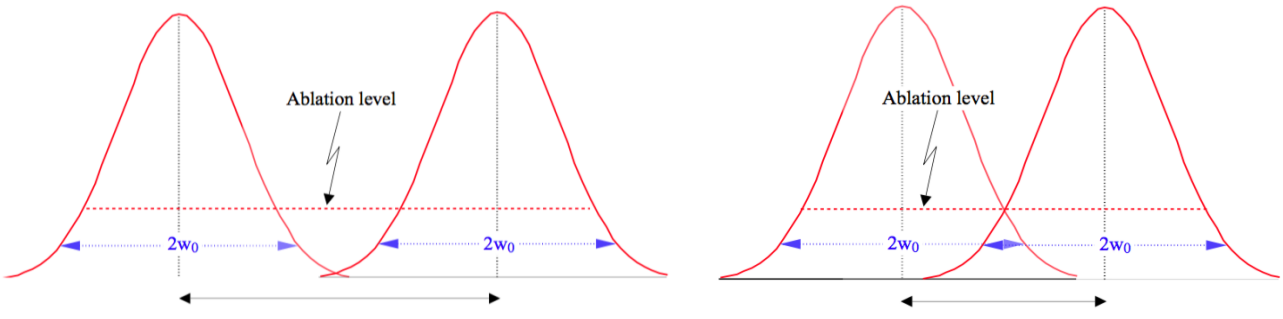

G40: XY grid spacing > $2w_0 \approx 30$ µm

G25: XY grid spacing < $2w_0 \approx 30$ µm

Fig. 1. G40 and G25 grid spacing of the Gaussian laser beam (waist $2w_0$). According to the ablation level and the beam overlap, the surface should not be textured in the middle part with the G40 grid, unlike the G25 grid.

The fabricated G25 grid had round-contoured protrusions (Fig. 2a to 2c), whereas the G40 grid had squarer contours with protruding edges (Fig. 2e to 2g). A total of 40 scans was necessary to pattern trenches of around 15 µm deep. A 90% overlap was chosen for the laser shots, which corresponds to about 10 cumulated pulses per spot. The obtained multiscale structure is shown in the enlargements (Fig. 2c and 2g) where it can be seen that the submicrometer wavelength, well known as LIPSS (Laser Induced Periodical Surface Structures) covers all irradiated areas.

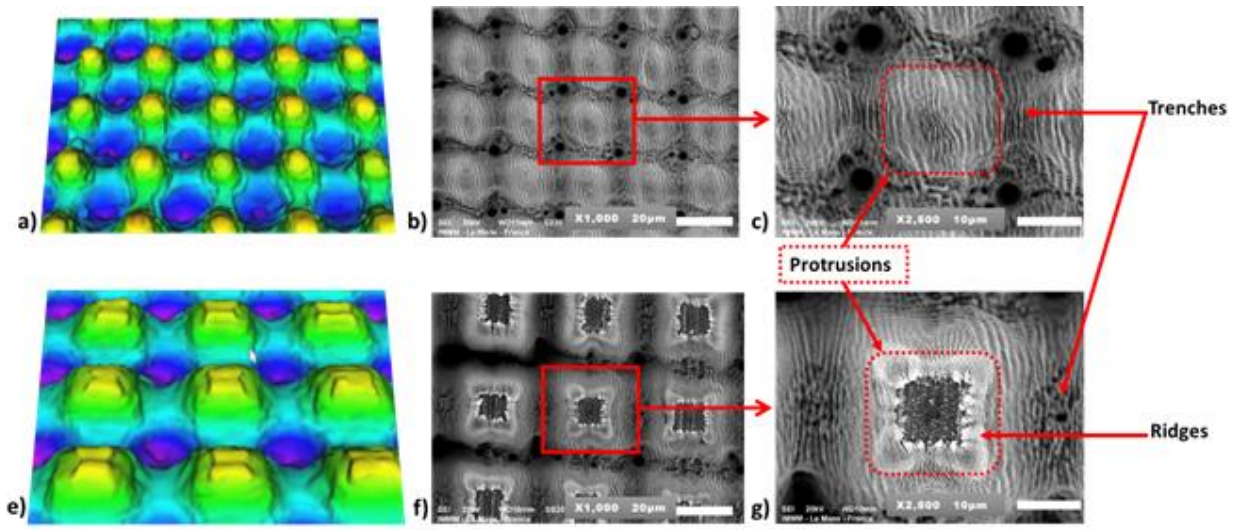

Fig. 2. Morphologic structure of femtosecond laser textured steel samples. The 3D profile of G25 substrate (a), with its corresponding SEM picture at x1000 (b) and x2500 magnification (c). The 3D profile of G40 substrate (e), with its corresponding SEM picture at x1000 (f) and x2500 magnification (g).

After the laser texturing process followed by cleaning in an ultrasonic bath, the samples were stored in ambient air at 40% RH, and regularly tested for wettability. Some of them were measured every hour, others once a day.

2.3. Surface characterization techniques

Substrate roughness and topography were measured with a 3D profilometer (InfiniteFocus, Alicona Imaging GmbH, Austria). The XY horizontal resolution can reach 0.5 µm while the vertical Z resolution is about 10 nm. Using the focus variation method in white light and a limited depth of field optical system, a numerical reconstitution was achieved to study the micrometrical scale surface structures.

Morphologic surface characterization was carried out using a scanning electron microscope (SEM, JEOL, JSM 6510LV) coupled with energy dispersive spectroscopy (EDS). All spectra were obtained with a 2048x1536 format resolution at 10kV, with an average of 10 runs of 4 min each.

Chemical surface characterization was performed with an X-ray Photoelectron Spectroscopy (XPS) instrument (Kratos Axis Nova, Analytical, Manchester, UK, Institut des Matériaux de Nantes, France) with the monochromatic Al Kα beam and an electron emission angle of 90° relative to the sample surface. The pass energies for survey spectra were 80 eV (0.5 eV increment). Background linear subtraction was performed, and the resolution fitting accuracy was 5%. The quantification of XPS spectra was performed with the CasaXPS software (Casa Software Ltd.). XPS analysis allowed the determination of the surface atomic composition. Measurements were performed on multiple substrates, textured at different periods of time. Due to measurement delay, the analysis was focused on the quantitative XPS spectra.

Raman spectra of samples were also performed with a LabRam ARAMIS spectrometer (Horyba Jobin Yvon, France) in ambient air. The spectra were excited with 632.8 nm radiation from 100 cm^{-1} to 1550 cm^{-1} with a resolution around 2 cm^{-1}. The scans were obtained for 20 s each at a 500 cm^{-1} step size. The laser beam was focused on the substrate to obtain a spot size of 10 µm in diameter. The power was reduced below 0.4 mW to avoid sample degradation.

In order to evaluate the wetting properties, the WCA was measured using the sessile drop method [25] by means of an automated optical tensiometer (Attension Theta Lite, Biolin Scientific, Sweden). The WCA of ultra pure water 2µL droplet was numerically captured and calculated by the embedded OneAttension software. Each WCA was measured three times on different areas of the same sample, and on three different samples bearing the same texture. Then, the average values were used. Since water droplets had the tendency to spread onto the textured surface, in particular a few hours after laser interaction, the WCA measurements were immediately taken owing to the video camera. Also, in order to take the fact that several 2 µL droplets could not stick to the surface, the corresponding samples were considered as superhydrophobic.

3. Results

3.1. Contact angle measurements

In order to highlight the role of the ultrasonic cleaning after laser texturing, two series of samples are studied: one with post-interaction US cleaning, and the other without. The evolution of WCA for the two substrates G25 and G40 is shown in Fig. 3.

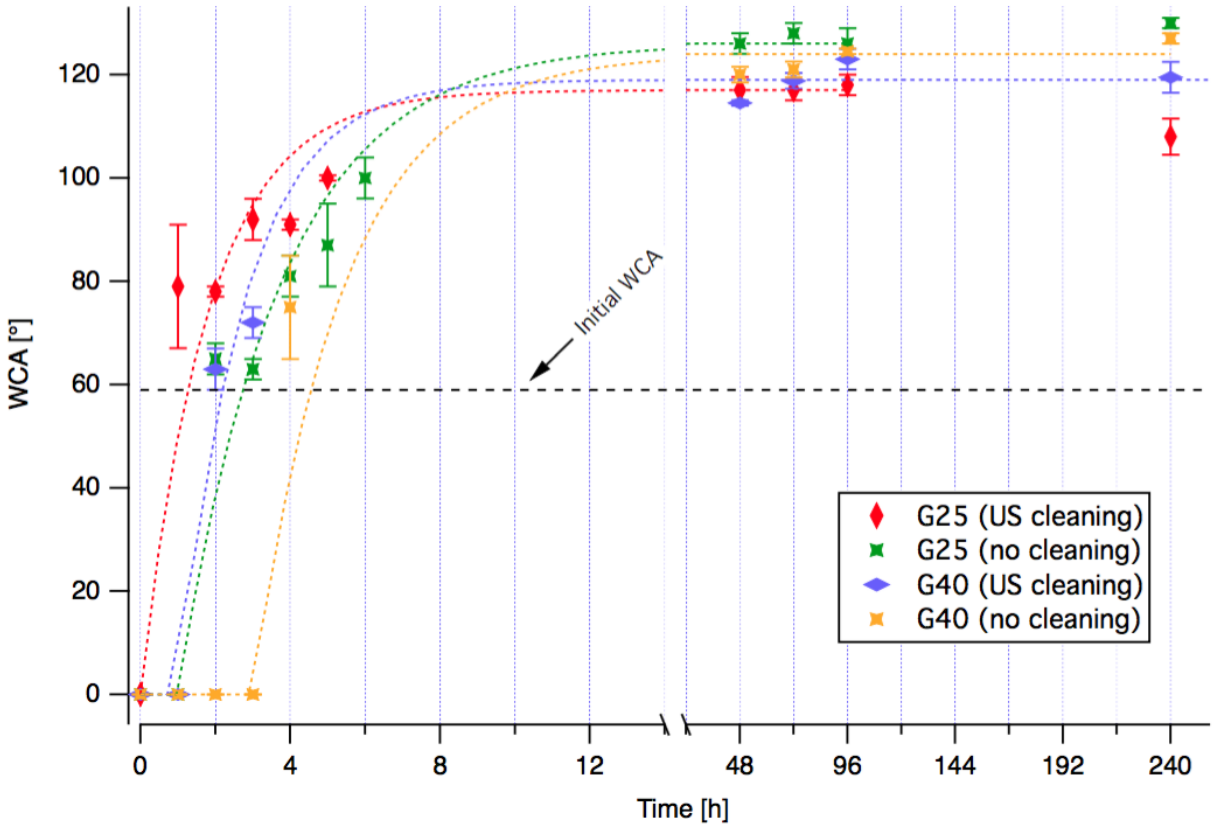

Fig. 3. Dependence on ageing time of the G25 and G40 wettability with or without ultrasonic cleaning. The dash line at 59° shows the initial WCA of a reference non-textured substrate.

The non-textured reference sample has a WCA of about 59 ± 3°, independently of the cleaning. Immediately after texturing, and regardless of the texturing conditions, substrates are totally hydrophilic (WCA ≈ 0°) up to 3 hours after irradiation. A few hours later, depending on the conditions, their respective WCA evolves rapidly to reach a plateau around 120°, i.e. almost 60° higher than the reference sample. However, the deposited drops are not stable during the

measurement; they spread down rapidly, inducing high standard deviations during the first few hours, (Fig. 3). As a first approach, the curves can be fitted by a first order time evolution following

$$WCA = A\left[1 - \exp(-\frac{t - t_0}{\tau})\right] \qquad t > t_0$$

where A represents the WCA asymptotic value, τ the time constant, and t_0 the time delay. Table 3 summarizes the values of τ and A for both G25 and G40 substrates.

Table 3. Time constants τ and WCA asymptotic values A for different substrates and cleaning conditions.

Substrate	G25		G40	
Cleaning	US	NO	US	NO
τ (h)	1.8 ± 0.35	2.7 ± 0.4	1.73 ± 0.2	2.4 ± 1.16
A (°)	117 ± 5.6	126 ± 5	119 ± 8.5	124 ± 7.3

Time constant values are from around 1.7 h with US cleaning (G40) to about 2.7 h without (G25). For an equivalent energy density, A.M. Kietzig *et al*. report similar time constants on steel surface [18]. Cleaning of the samples yields? a lower time constant, and G40 substrates have a slightly faster kinetics than G25 substrates. WCA asymptotic values A varies from around 118° with US cleaning (G25) to about 126° (G25) without. Cleaning the samples results in a lower asymptotic WCA value ranging from 126° down to 117° (G25) and from 124° down to 119° (G40), i.e. a reduction of about 5° to 9°. Nevertheless, the G25 or G40 substrates exhibit no significant differences. All the studied substrates reach a superhydrophobic state after 2 or 4 months of storage. Indeed, the drops are repulsed and cannot stick to the surfaces. Moreover, cleaning any aged textured sample in an ultrasonic bath makes the substrate hydrophilic with its initial WCA, and in some cases, the substrate even becomes superhydrophobic after one month.

3.2. Raman analysis

The Raman analysis was performed in the first hours of maturation when the textured substrate was still fully wetting, in order to detect any surface heterogeneity. The spectrum of untreated steel shows no vibration bands in the studied wave number range from 100 cm^{-1} to 1500 cm^{-1} (Fig 4, a. curve). As a result, no trace of oxidation on the surface of the material is detected.

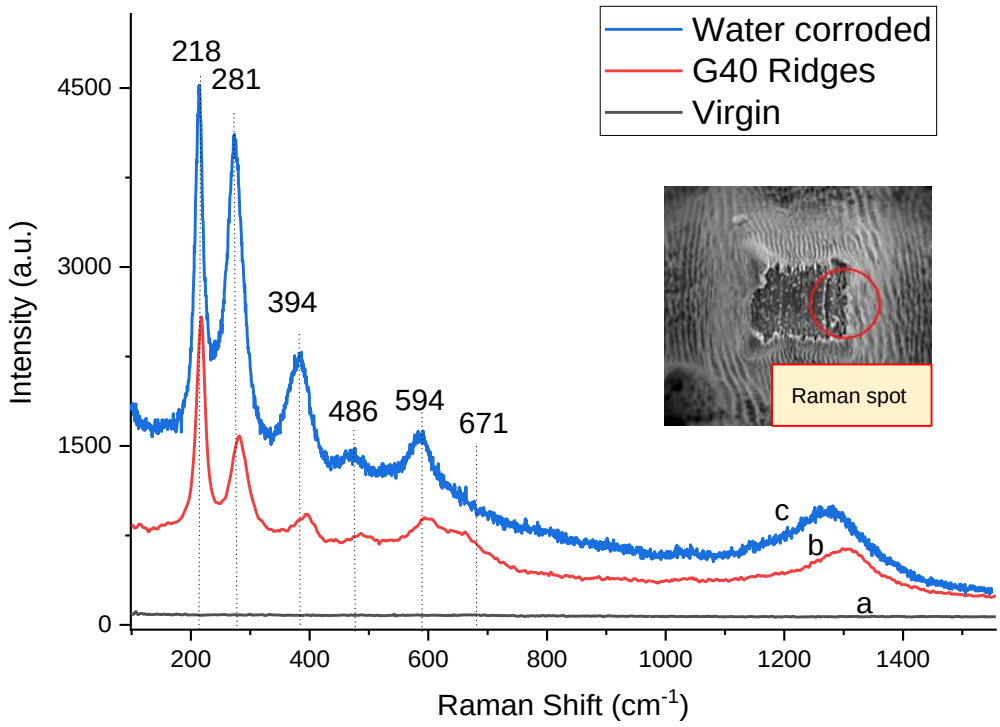

Fig. 4. Comparison of Raman spectra of 3 different steel surfaces: (a) Virgin sample, (b) ridge of a femtosecond laser textured protrusion a few hours after the laser treatment, (c) corroded sample in distilled water for 5 days.

The spectrum corresponding to the ridges of G40 substrate (Fig 4, b. curve), shows narrow bands (218, 281, 394, 486, 594 and 671 ± 1 cm^{-1}) assigned to the hematite (α-Fe_2O_3) [26], [27], the most common and stable phase of iron oxide III. The broad band around 1300 cm^{-1} is associated to a collective spin movement [27]. All these bands are also observed on a steel sample immersed in distilled water for 5 days (Fig 4, c. curve). Hematite is therefore the main element in the corrosion layer developed on the surface.

From the laser patterning and its Gaussian profile (Fig. 1), it can be observed that the G40 ridges were formed by a low energy density, probably at the same level of thermal treatment. Closer to the beam center, the interaction rather corresponds to laser ablation without any thermal oxidation. The G40 trench is therefore formed at high energy, and its Raman signature (Fig 5, a. curve) is compared to those of the entire G25 surface (Fig 5 b and c). Despite the slight energy distinction that can be made between the high energy of the beam center for trenches and the lower energy density that forms G25 protrusions (with pitch scans overlapped by 20%), the three Raman spectra show the same broad band between 450 - 730 cm^{-1} with a maximum at 662 cm^{-1} of varying intensity corresponding to the formation of magnetite (Fe_3O_4) even if the wüstite cannot be clearly excluded, as described in [27], because of the band broadness [26-28]. The presence of the same oxide under different texturing conditions allows us to state that energy distribution is a major factor in the formation of oxide on the surface sample.

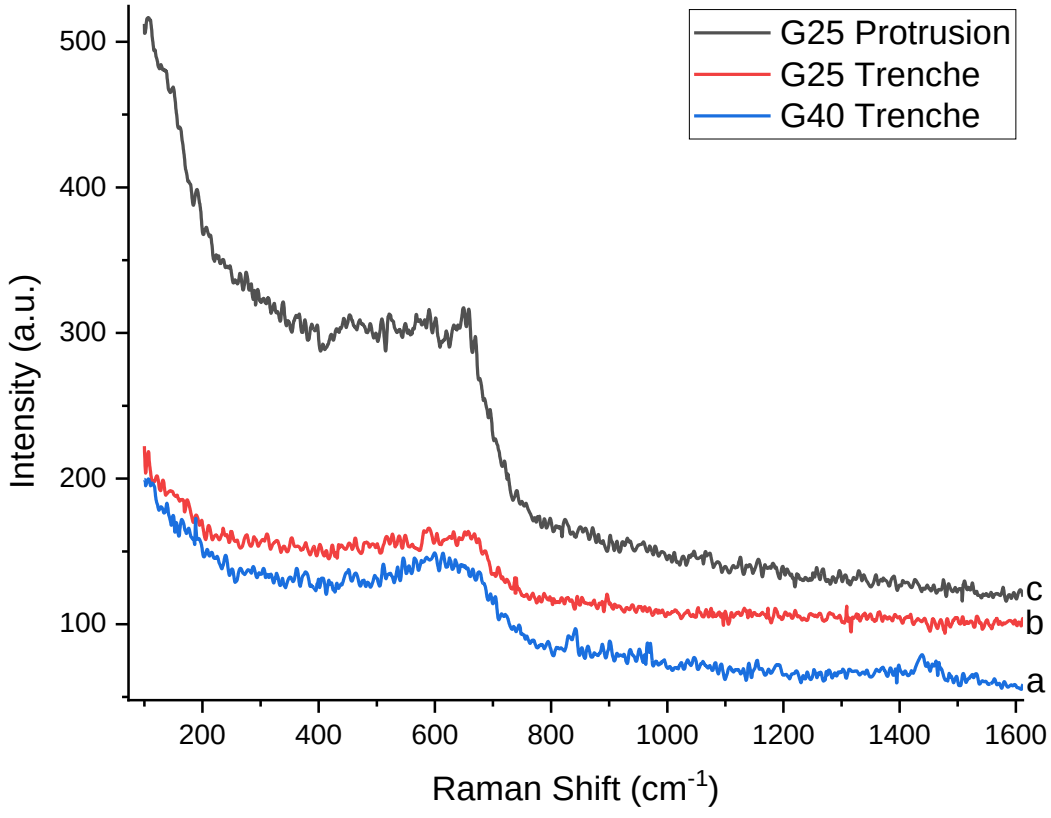

Fig. 5. Comparison of Raman spectra for the magnetite peak (Fe_3O_4 662cm^{-1}) in different locations of a textured substrate: (a) G40 trench, (b) G25 trench, (c) G25 protrusion.

3.3. XPS Analysis

XPS is used to determine the elemental composition of the sample for both G25 and G40 patterns, after 2, 5 and 15 days of maturation. As expected, XPS survey spectra (Fig. 6) reveal peaks at 284.9 eV corresponding to C1s, 529.9 eV for O1s and 710.9 eV for Fe2p core electrons on both patterned structures. Other elements such as Ca2p (at 347.4 eV) and Co2p (at 782.9 eV) are sometimes detected as traces and are therefore neglected. The G40 spectra for all maturation states (Fig. 6) show that femtosecond laser irradiation led to a substantial and progressive alteration of chemistry (G25 spectra are identical to G40 spectra). Indeed, the reference C1s peak shows 3 different substructures (C-C/C-H at 285 eV, C-O at 286.4 eV and C=O at 288.8 eV) whose proportions decrease after the maturation. The decrease of carbon contamination after maturation is confirmed by the FeO (FeO, Fe_2O_3 or Fe_3O_4) structure at 530 eV in the aged sample while the O1s peak for the virgin sample presents the two substructures (FeO and C-O at 532 eV). The Fe2p peak of the reference sample is composed of two components, the Fe metal at 707 eV and Fe^{3+} at 711 eV and this peak after maturation is only characteristic of the Fe^{3+} structure. Therefore, the formation of wüstite can be excluded.

All the normalized atomic percentages are summarized in Fig 7. The atomic percentage of the virgin sample (marked as 0) was 50.5 ± 2.2% for C1s and 34.1 ± 1.2% for O1s and 15.4 ± 1.4% for Fe 2p. For each surface structure, we notice an increasing proportion of oxygen (red curve) until the 15^{th} day of ageing with 49.9 ± 1.5% for G25 and 48.3 ± 3.8% for G40, and a decrease of carbon (blue curve) of 36.0 ±1.0% for G25 and 34.8 ± 6.8% for G40 as observed in Bizi-Bandoki *et al.* [17]. According to Divin-Mariotti *et al.* [20], the ablation process of several micrometers deep of stainless steel implies a significant decontamination of the extreme surface and the appearance of a highly reactive surface. In our case (40CMD8+S steel), a similar process may occur and it becomes more significant in the case of full irradiated sample G25. In addition, the plateau values of all the involved elements at the 15^{th} day past laser irradiation are relatively close for G25 and G40 substrates, as shown in Fig. 7.

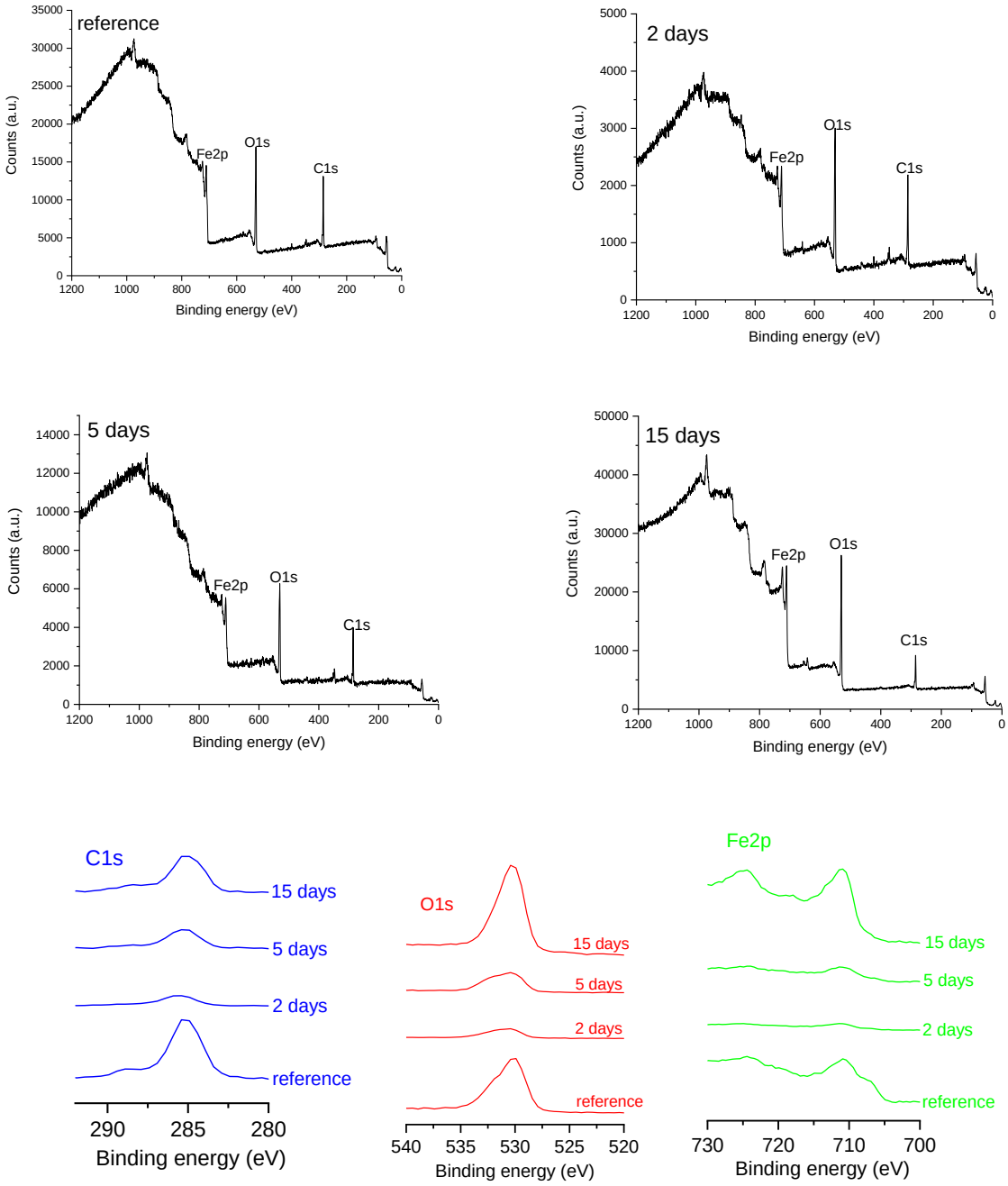

Fig. 6. Comparison of XPS survey spectra over ageing time of 2, 5 and 15 days for 40µm patterning structures (G40) and blank sample.

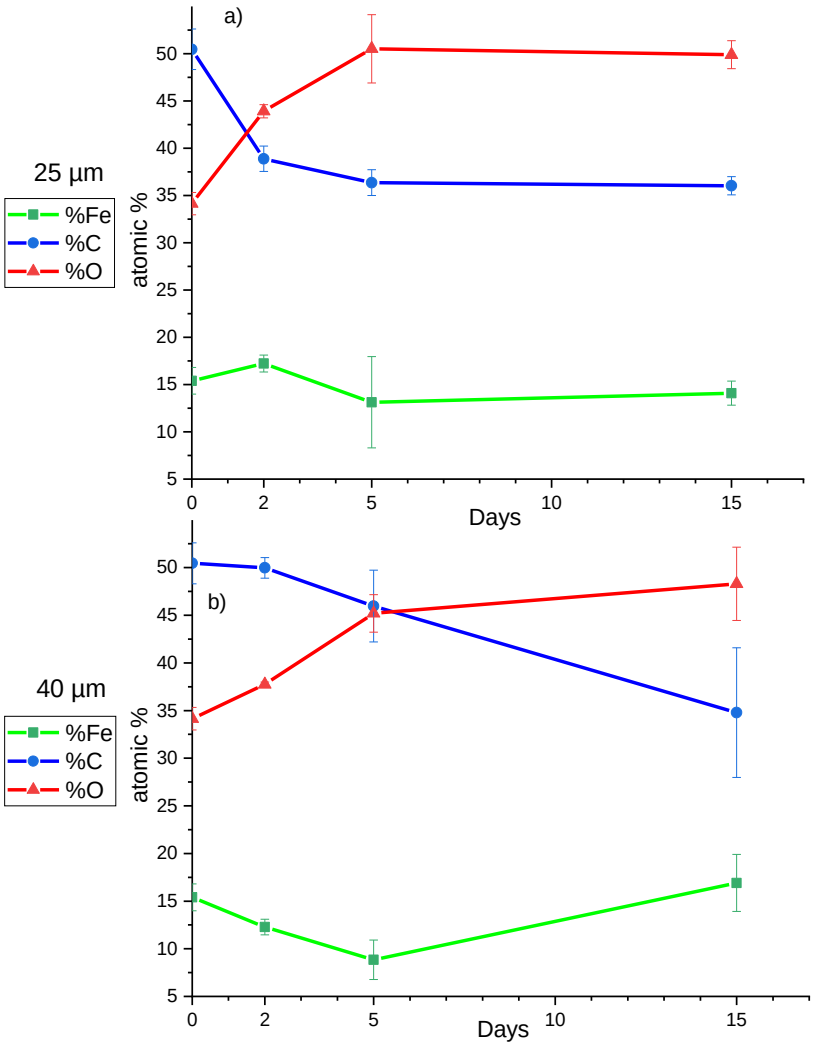

Fig. 7. Dependence of atomic proportions of iron, carbon and oxygen (issued from XPS spectra) on ageing duration for G25 (a) and G40 (b).

3.4. EDX analysis

EDX mapping for the three elements was performed on textured samples aged in ambient humid air over 15 days (Fig. 8). The images highlight the distribution of the concentration of iron (in green), carbon (in blue), and oxygen (in red) for both patterns. SEM (a) and EDX (b to d) images are shown for G25 patterns (Fig 8-1) and for G40 patterns (Fig 8-2). The horizontal dark strips on the colored EDX pictures are caused by the angle of the incident X-ray. For G40 samples, the singular location of oxygen in a square shape indicates a high level of oxidation whereas the concentration of iron in the same area is decreased. In contrast, G25 samples generate a uniform

distribution on nearly all the elements. One may observe the slightly brighter oxygen concentration at the protrusion spot explained by the distribution in deposited energy due to the Gaussian profile of the beam. This implies that the choice of a specific laser patterning strongly affects the surface chemistry.

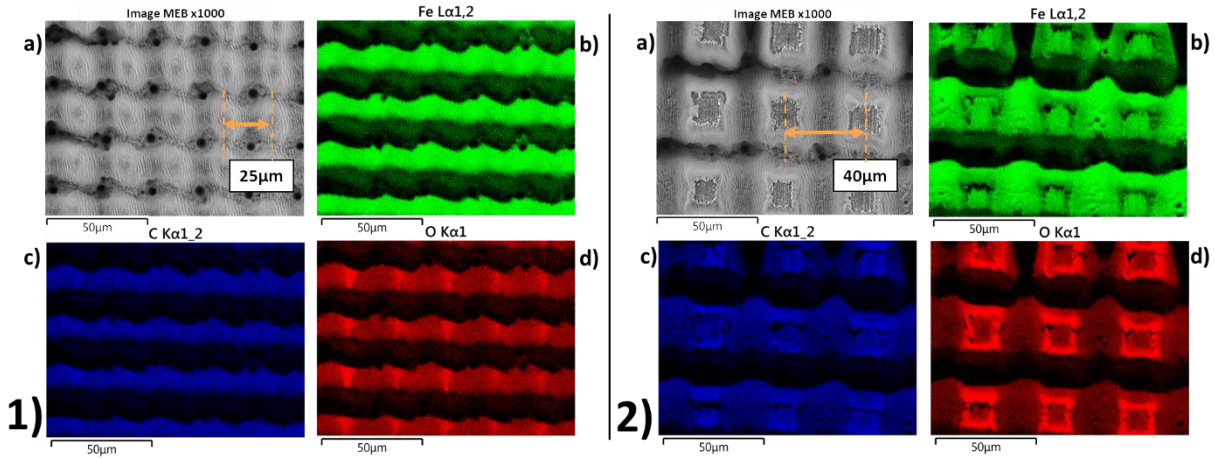

Fig. 8. SEM picture (a) and their corresponding EDX mapping (b to d) of the G25 (1) and G40 (2) patterns for each main element, 15 days after laser texturing.

Considering the theoretical composition of the 40CMD8+S issued from the datasheet (Table 1), 95.95% of the bulk is composed of iron, 0.40% of carbon and no oxygen. Obviously, the EDX analysis of virgin sample (1µm deep only) in the same area as the EDX mapping, shows a different chemistry, with a surface composition of iron 85.1 ± 1.0%, carbon 10.1 ± 1.0%, and oxygen 1.0 ± 0.2% (see Fig 9). The proportions of other elements (e.g. Mn, Cr, or Si) are not relevant.

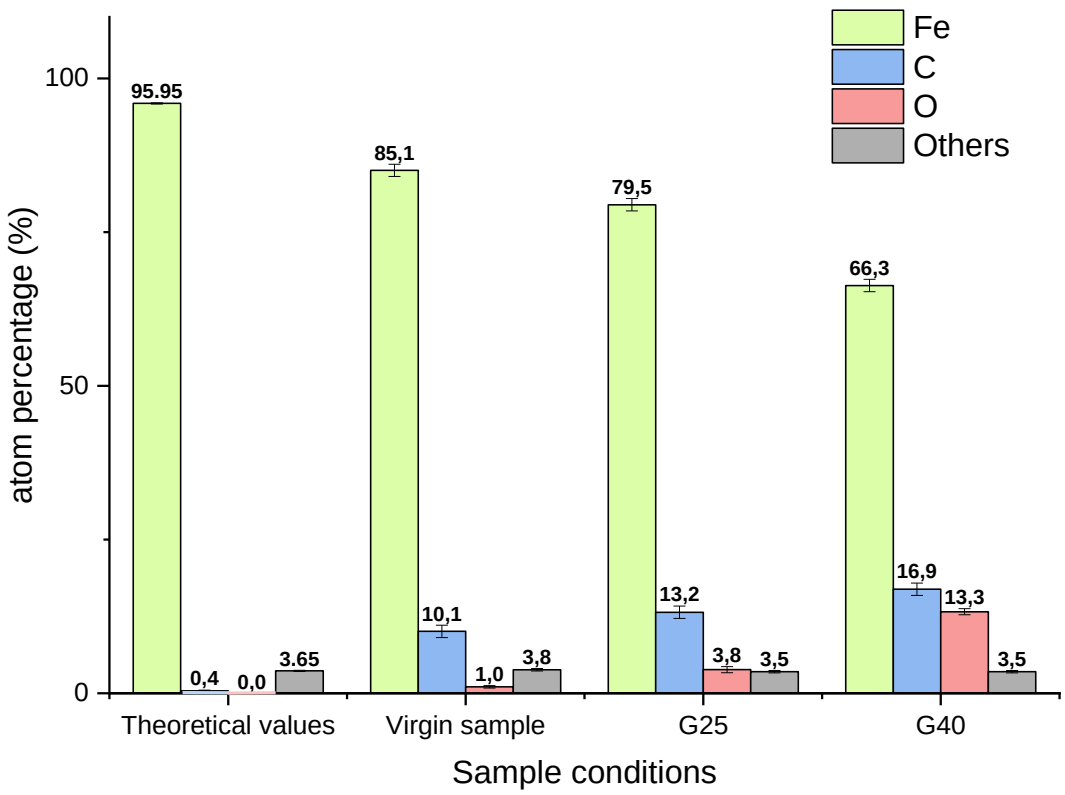

Fig. 9. Elemental percentage of iron, carbon and oxygen at the surface extracted from EDX mapping (Fig. 8) of the samples in different states compared to the datasheet values of 40CMD8+S. Virgin surface and two different laser patterning samples after 15 days of ageing.

For both G25 and G40, because of the oxidation induced by laser interaction, the presence of oxygen increases. From Fig. 9, G40 samples has a more oxidized surface than the virgin steel surface by 13 times; for the G25, it is about (only) 4 times. These differences might be associated with the internal oxidation zone (under the border of the G40 ridges) compatible with the penetration length of EDX incident X-rays [29].

The amount of carbon located on the surface also rises after laser irradiation and is more significant for the G40 (16.5 ± 1.0%) than for G25 (13.5 ± 1.0%). This can be explained by the enhancement of C diffusion due to a low fluence at the edge of the Gaussian beam that leads to thermal effect [30]. The lower the fluence below the ablation threshold, the bigger the thermal effect, thus followed by carbon diffusion.

4. Discussion

Most of the papers dealing with wettability survey on ageing after laser texturing, report a so-called steady state, where WCA no longer evolves [14], [20]. Our first results indicate the same trend since the WCA is constant between 4 and 30 days. However, there is an apparent contradiction with the superhydrophobic phenomenon that occurs after a few months: as a matter of fact, it is appropriate to substitute the usual exponential regression by a double regression, one with a short time constant of a few hours, and a second one, more likely approaching several months.

To validate this hypothesis, one might explore long term analysis. Moreover, the reversibility of wettability condition, and hence the surface chemistry, after an ultrasonic cleaning, validate the reinterpretation of the steady state. The apparent phenomenon might be explained by an oxidation gradient over time along the thickness of the material.

According to the energetic distribution of the laser applied to G25 and G40 configurations, and their corresponding Raman spectra implying distinct chemistries, we expected a more significant difference between the measured contact angles. Nevertheless, the quantitative XPS results of the involved elements of the extreme surface, show similar percentages for both patterns. The slight variation between the time constants of the two pitch grid substrates (Table 3) may be due to hematite presence on G40 ridges slowing down the chemical surface reorganization. Indeed, G25 has been formed with a 20% overlap of the laser spots, so that the surface is essentially composed by magnetite. Also, when no ultrasonic cleaning is performed, time constants are almost doubled, supporting the idea of a slowdown in reorganization.

As most articles on the same material [18], [19], it can be found that G25 and G40 substrates evolve quickly hour after hour. However, time constants can be counted in days when different materials are used or when one of the laser parameters is changed. Indeed, industrial steels such as 40CMD8+S are not frequently studied; stainless steel is practically the only studied metal when it comes to laser processes ageing topic. It may also confirm the lack of steady states in our experiments. The XPS analysis allows for the calculation C1s/O1s ratio with an initial value of 1.5

before treatment, progressively decreasing to 0.72 for both patterning samples. Same values were already found on stainless steel by Divin-Mariotti *et al.* [20] but for a longer ageing duration (53 days) in similar atmospheric storage conditions. As a result, it seems that there is an equilibrium ratio of steel surface regardless of the kind of texturation. Therefore, one may conclude that the surface chemistry is prevalent, rather than the physical ablation; in this respect however, further investigation should be made.

Finally, Raman spectra show two kinds of surface oxidation type; for G25, only magnetite has been detected, and for G40, hematite has been spotted on protrusion ridges and magnetite on trenches. In order to have a further understanding of these distinct oxidation formation, we could consider Kietzig *et al.* model [18], in which laser interaction (with no further precision) induces the creation of active magnetite sites $Fe_3O_{4-\delta}$ ($0 < \delta < 1$) acting like a catalyst to CO_2 molecules in the dissociative adsorption. This model could explain the ageing of textured samples and the rise of the carbon amount, according to the 1µm deep EDX spectrum. However, it cannot justify the hematite on the ridge of G40 protrusions. Chourpa *et al*. [26], leads to a better understanding of laser and oxide structures behaviors. They proceed to an invasive Raman analysis on a material called black iron oxide; in other terms, they used a laser power above the oxidation threshold. This material contains a mixture of hematite and magnetite. The Raman spectrum reveals hematite and laser-induced hematite due to magnetite oxidation. This common phenomenon of magnetite alteration into hematite is called martitization [27], [31]. An intermediary unstable oxide, maghemite (γ-Fe_2O_3), can be formed according to the following phase transition [27]:

$$Fe_3O_4 \xrightarrow{200\,^\circ C} \gamma - Fe_2O_3 \xrightarrow{400\,^\circ C} \alpha Fe_2O_3$$

A possible explanation for hematite presence in G40 ridges, would involve a martitization of the induced active magnetite sites as described by Kietzig *et al.* model [18]. Because of the low energetic profile of the border of the Gaussian beam, there is not sufficient energy density to perform laser ablation. Nevertheless, knowing the high repetition rate of the laser inducing thermal accumulation [32], it may be sufficient to chemically alter the structure above 400°C and to take part in hematite formation. Femtosecond lasers has an extremely low thermal effect, so that laser

ablation is the only phenomenon that occurs in G25, hence, it could explain why magnetite is the only oxide that remains.

5. Conclusion

It has been shown that texturing grid patterns on a 40CMD8+S steel with a femtosecond laser leads to a decrease of carbon and an increase of oxygen proportion on the extreme surface. Ageing from hydrophilic to hydrophobic behavior was made possible by the constant oxidation mechanism due to the humid ambient air of around 40% RH. However, the Gaussian profile of the laser implied that, on the first micrometers of the substrate, carbon amount increased due to carbon diffusion induced by the low energy density region of the beam causing a thermal effect. Oxygen proportion also increases in this area. One of the main cause of this oxidation was established with the study of Raman spectrum on the ridges and the trenches. It has been shown that the laser generates active magnetite sites on which the martitization process occurs when thermal energy is induced; it explains also why these low density zones are mainly hematite based, and why ablation leads to magnetite surface chemistry. Steel surfaces have their own maturation mode when wettability is focused. It allows for the development of more than one regression curve in order to explain the absence of a steady state after sufficient ageing time, and the short value of the time constant compared with most of the authors' observations made on stainless steel. In the future, long duration ageing surveys would be interesting, in order to determine precisely the time constant of the second exponential and when the steady state is more likely to appear on laser textured steel samples. Also, a laser interaction modeling taking into account the thermal part of the Gaussian beam is currently studied. In this way, a better understanding of laser induced oxidation will be proposed.

Acknowledgement

We thank the French ICUBE research institute for the assistance with the Raman experiment and for providing us with relevant assistance and advice. This study is part of the FUI project "NEME" supported by the French agency ANRT. The authors wish to acknowledge and

to associate the industrial and academic partners of this project; respectively Hutchinson, Meliad, Stacem, Capacités and IREPA LASER. We thank IREPA LASER and the ANRT for funding the PhD scholarship.

Data availability

The data reported in this manuscript are available from the corresponding author on a reasonable request.

Declarations

Conflicts of Interest The authors declare that they have no conflict of interest.

References

[1] Barthlott W., Neinhuis C. (1997) Purity of the sacred lotus, or escape from contamination in biological surfaces, Planta 202(1) 1-8.
[2] Liu Y., Bai Y., Jin J., Tian L., Han Z., Ren L. (2015) Facile fabrication of biomimetic superhydrophobic surface with anti-frosting on stainless steel substrate, Appl. Surf. Sci. 355 1238-1244. https://doi.org/10.1088/1361-665X/aadb6
[3] Schutzius T.M., Bayer I.S., Jursich G.M., Das AMegaridis., C.M. (2012) Superhydrophobic–superhydrophilic binary micropatterns by localized thermal treatment of polyhedral oligomeric silsesquioxane (POSS)–silica films, Nanoscale 4(17) (2012) 5378. https://doi.org/10.1039/c2nr30979c
[4] Marchand D.J., Dilworth Z.R., Stauffer R.J., Hsiao E., Kim JH., Kang JG., Kim SH., (2013) Atmospheric rf plasma deposition of superhydrophobic coatings using tetramethylsilane precursor, Surf. Coat. Technol. 234 14-20, 2013. https://doi.org/10.1016/j.surfcoat.2013.03.029
[5] Palumbo F., Di Mundo R., Cappelluti D., d'Agostino R. (2011) Superhydrophobic and Superhydrophilic polycarbonate by tailoring chemistry and nano-texture with plasma processing, Plasma Process. Polym. 8(2) 118-126. https://doi.org/10.1002/ppap.201000098
[6] Chen L.J., Chen M., Zhou H.D., Chen J.M. (2008) Preparation of super-hydrophobic surface on stainless steel, Appl. Surf. Sci. 255(5) 3459-3462. https://doi.org/doi: 10.1016/j.apsusc.2008.07.122.
[7] Barbieri L., Wagner E., Hoffmann P. (2007) Water wetting transition parameters of perfluorinated substrates with periodically distributed flat-top microscale obstacles, Langmuir 23(4) 1723-1734. https://doi.org/10.1021/la0617964
[8] Kam D.H., Bhattacharya S., Mazumder J. (2012) Control of the wetting properties of an AISI 316L stainless steel surface by femtosecond laser-induced surface modification, J. Micromec. Microeng. 22(10) 105019. https://doi.org/10.1088/0960-1317/25/4/045007
[9] Kwon M.H., Shin H.S., Chu C.N. (2014) Fabrication of a super-hydrophobic surface on metal using laser ablation and electrodeposition, Appl. Surf. Sci. 288 (2014) 222-228. https://doi.org/10.1016/j.apsusc.2013.10.011

[10] Li B.J., Li H., Huang L.J., Ren N.F., Kong X. (2016) Femtosecond pulsed laser textured titanium surfaces with stable superhydrophilicity and superhydrophobicity, Appl. Surf. Sci. 389 585-593. https://doi.org/10.1016/j.apsusc.2016.07.137
[11] Luo B.H., Shum P.W., Zhou Z.F., Li K.Y. (2010) Preparation of hydrophobic surface on steel by patterning using laser ablation process, Surf. Coat. Technol. 204(8) 1180-1185, 2010. https://doi.org/10.1016/j.surfcoat.2009.10.043
[12] Moradi S., Kamal S., Englezos P., Hatzikiriakos S.G. (2013) Femtosecond laser irradiation of metallic surfaces: effects of laser parameters on superhydrophobicity, Nanotechnology, 24(41) 415302.
[13] Li W., Amirfazli A. (2005) A thermodynamic approach for determining the contact angle hysteresis for superhydrophobic surfaces, J. Colloid Interface Sci. 292(1) 195-201.
[14] Ta V.D., Dunn A., Wasley T.J., Li J., Kay R.W., Stringer J., Smith P.J., Esenturk E., Connaughton C., Shephard J.D. (2016) Laser textured superhydrophobic surfaces and their applications for homogeneous spot deposition, Appl. Surf. Sci. 365 153-159. https://doi.org/10.1016/j.apsusc.2016.01.019
[15] Jagdheesh R., Diaz M., Marimuthu S., Ocaña J.L. (2019) Hybrid laser and vacuum process for rapid ultrahydrophobic Ti-6Al-4 V surface formation, Appl. Surf. Sci. 471 759-766. https://doi.org/10.1016/j.apsusc.2018.12.047
[16] Bizi-Bandoki P., Benayoun S., Valette S., Beaugiraud B., Audouard E. (2011) Modifications of roughness and wettability properties of metals induced by femtosecond laser treatment, Appl. Surf. Sci. 257(12) 5213-5218. https://doi.org/ 10.1016/j.apsusc.2010.12.089
[17] Bizi-bandoki P., Valette S., Audouard E., Benayoun S. (2013) Time dependency of the hydrophilicity and hydrophobicity of metallic alloys subjected to femtosecond laser irradiations, Appl. Surf. Sci. 273 399-407. https://doi.org/10.1016/j.apsusc.2013.02.054
[18] Kietzig A.M., Hatzikiriakos S.G., Englezos P. (2019) Patterned Superhydrophobic Metallic Surfaces, Langmuir 25(8) 4821-4827. https://doi.org/10.1021/la8037582
[19Kietzig] A.M., Mirvakili M.N., Kamal S., Englezos P., Hatzikiriakos S.G. (2011) Laser-patterned super-hydrophobic pure metallic substrates: cassie to wenzel wetting transitions, J. Adhes. Sci. Technol. 25(20) 2789-2809. https://doi.org/10.1163/016942410X549988
[20] Divin-Mariotti S., Amieux P., Pascale-Hamri A., Auger V., Kermouche G., Valiorgue F., Valette S. (2019) Effects of micro-knurling and femtosecond laser micro texturing on aluminum long-term surface wettability, Appl. Surf. Sci. 479 344-350. https://doi.org/10.1016/j.apsusc.2019.02.025
[21] Calderon M., Rodríguez A., Dias-Ponte A., Morant-Minana M.C., Gómez-Aranzadi M., Olaizola S.M. (2016) Femtosecond laser fabrication of highly hydrophobic stainless steel surface with hierarchical structures fabricated by combining ordered microstructures and LIPSS, Appl. Surf. Sci. 374 (2016) 81-89. https://doi.org/10.1016/j.apsusc.2015.09.261
[22] Ngo C.V., Chun D.M. (2017) Fast wettability transition from hydrophilic to superhydrophobic laser-textured stainless steel surfaces under low-temperature annealing, Appl. Surf. Sci. 409 232-240. https://doi.org/10.1016/j.apsusc.2017.03.038
[23] Kim D., Kim J.G., Chu C.N. (2016) Ageing effect on the wettability of stainless steel, Mater. Lett. 170 18-20. https://doi.org/10.1016/j.matlet.2016.01.107
[24] Long J., Zhong M., Fan P., Gong D., Zhang H. (2015) Wettability conversion of ultrafast laser structured copper surface, J. Laser Appl. 27(S2) S29107.
[25] Anastasiadis S.H., Hatzikiriakos S.G. (1998) The work of adhesion of polymer/wall interfaces and its association with the onset of wall slip, J. Rheology 42(4) 795-812.

[26] Chourpa I., Douziech-Eyrolles L., Ngaboni-Okassa L., Fouquenet JF., Cohen-Jonathan S., Soucé M., Marchais H., Dubois P. (2005) Molecular composition of iron oxide nanoparticles, precursors for magnetic drug targeting, as characterized by confocal Raman microspectroscopy, Analyst 130(10) 1395-1403.
[27] de Faria D.L.A., Venâncio Silva S., de Oliveira M.T. (1997) Raman microspectroscopy of some iron oxides and oxyhydroxides, J. Raman Spectrosc. 28(11) 873-878.
[28] Thibeau R.J., Brown C.W., Heidersbach R.H. (1978) Raman spectra of possible corrosion products of iron, Appl. Spectrosc. 32(6) 532-535.
[29] S. Canli, Thickness analysis of thin films by energy dispersive X-ray spectroscopy" (PhD), Middle East Technical University, p. 93.
[30] Antonio G.G., Jean-Michel R., Yana L., Behnam D., Hanshan D., Pavel P., Stefan D. (2018) Combined surface hardening and laser patterning approach for functionalising stainless steel surfaces, Appl. Surf. Sci. 439 516-524. https://doi.org/10.1016/j.apsusc.2018.01.012
[31] P. Ramdohr, The ore minerals and their intergrowths. Oxford; Toronto: Pergamon Press, 1969.
[32] C. Hairaye, Fonctionnalisation de surfaces par microstructuration laser, (PhD), Université de Strasbourg, 2017, p.95.